

UNCLASSIFIED

**Defense Technical Information Center
Compilation Part Notice**

ADP014794

TITLE: Numerical Simulation of Protoplanetary Vortices

DISTRIBUTION: Approved for public release, distribution unlimited

This paper is part of the following report:

TITLE: Annual Research Briefs - 2003 [Center for Turbulence Research]

To order the complete compilation report, use: ADA420749

The component part is provided here to allow users access to individually authored sections of proceedings, annals, symposia, etc. However, the component should be considered within the context of the overall compilation report and not as a stand-alone technical report.

The following component part numbers comprise the compilation report:

ADP014788 thru ADP014827

UNCLASSIFIED

Numerical simulation of protoplanetary vortices

By H. Lin, J.A. Barranco † AND P.S. Marcus ‡

1. Introduction

The fluid dynamics within a protoplanetary disk has been attracting the attention of many researchers for a few decades. Previous works include, to list only a few among many others, the well-known α -prescription of Shakura & Sunyaev (1973), the convective and instability study of Stone & Balbus (1996) and Hawley *et al.* (1999), the Rossby wave approach of Lovelace *et al.* (1999), as well as a recent work by Klahr & Bodenheimer (2003), which attempted to identify turbulent flow within the disk. The disk is commonly understood to be a thin gas disk rotating around a central star with differential rotation (the Keplerian velocity), and the central quest remains as how the flow behavior deviates (albeit by a small amount) from a strong balance established between gravitational and centrifugal forces, transfers mass and momentum inward, and eventually forms planetesimals and planets.

In earlier works (Barranco & Marcus 2000; Barranco *et al.* 2000; Lin *et al.* 2000) we have briefly described the possible physical processes involved in the disk; we have proposed the existence of long-lasting, coherent vortices as an efficient agent for mass and momentum transport. In particular, Barranco *et al.* (2000) provided a general mathematical framework that is suitable for the asymptotic regime of the disk; Barranco & Marcus (2000) addressed a proposed vortex-dust interaction mechanism which might lead to planetesimal formation; and Lin *et al.* (2002), as inspired by general geophysical vortex dynamics, proposed basic mechanisms by which vortices can transport mass and angular momentum. The current work follows up on our previous effort. We shall focus on the detailed numerical implementation of our problem. We have developed a parallel, pseudo-spectral code to simulate the full three-dimensional vortex dynamics in a stably-stratified, differentially rotating frame, which represents the environment of the disk. Our simulation is validated with full diagnostics and comparisons, and we present our results on a family of three-dimensional, coherent equilibrium vortices.

2. Governing equations

Scaling issues have been discussed in both Barranco *et al.* (2000) and Lin *et al.* (2002), and shall not be repeated. Here we simply list the governing equations that we propose to solve numerically, namely

$$\frac{\partial \bar{\rho} \mathbf{v}}{\partial t} + \bar{\rho} (\mathbf{v} \cdot \nabla \mathbf{v}) = -2\bar{\rho} \Omega_o \mathbf{z} \times (\mathbf{v} - \bar{\mathbf{v}}) - \nabla \tilde{p} - \bar{\rho} \Omega_o^2 z \mathbf{z}, \quad (2.1)$$

$$\nabla \cdot (\bar{\rho} \mathbf{v}) = 0, \quad (2.2)$$

$$\frac{\partial T}{\partial t} + \mathbf{v} \cdot \nabla T = -(\gamma - 1) T_o \left(1 + \frac{\tilde{p}}{\bar{p}}\right) \frac{v_z z}{H_o^2} - \frac{T}{\tau_{rad}(z)}, \quad (2.3)$$

† Department of Astronomy, University of California, Berkeley

‡ Department of Mechanical Engineering, University of California, Berkeley

$$\frac{\tilde{p}}{\bar{p}} = \frac{\tilde{\rho}}{\bar{\rho}} + \frac{\tilde{T}}{T_o}. \quad (2.4)$$

Here the equations are written in a rotating frame with an angular velocity Ω_o , x is the streamwise (ϕ) direction, y is the radial (r) direction, z is the direction about which the frame is rotating, and \mathbf{z} is its corresponding unit vector. In our notation system $\bar{\rho}$, \bar{p} , T_o and $\bar{\mathbf{v}}$ denote the base state density, pressure, temperature and velocity, respectively, and their forms will be given shortly. The tilde quantities $\tilde{\rho}$ and \tilde{p} denote the deviations of density and pressure from the base states, respectively, and γ is the ratio of specific heats. Finally H_o is the scale height of the disk and τ_{rad} is a radiation time scale. Compared with the governing equations (4.1-4.4) of Lin *et al.* (2002), we have further expanded the energy equation making use of the anelastic continuity equation (2.2); we have also linearized the equation of state to obtain equation (2.4) which is consistent with our current low-Mach number asymptotic regime.

We nondimensionalize equations (2.1-2.4) with the following scales:

$$[L] = H_o, \quad [\mathbf{v}] = c_s, \quad [t] = \frac{[L]}{[\mathbf{v}]} = \frac{1}{\Omega_o},$$

$$[\rho] = \rho_o, \quad [p] = \rho_o c_s^2 = p_o, \quad [T] = T_o,$$

where c_s is the speed of sound, ρ_o is a characteristic density, and T_o is the characteristic (base) temperature. The resulted *dimensionless* equations are

$$\frac{\partial \bar{\rho} \mathbf{v}}{\partial t} = -\bar{\rho}(\mathbf{v} \cdot \nabla) \mathbf{v} - 2\bar{\rho} \mathbf{z} \times (\mathbf{v} - \bar{\mathbf{v}}) - \nabla \tilde{p} - \bar{\rho} z \mathbf{z}, \quad (2.5)$$

$$\nabla \cdot (\bar{\rho} \mathbf{v}) = 0, \quad (2.6)$$

$$\frac{\partial T}{\partial t} = -\mathbf{v} \cdot \nabla T - (\gamma - 1) \left(1 + \frac{\tilde{p}}{\bar{p}} \right) v_z z - \frac{T}{\tau_{rad}(z)}, \quad (2.7)$$

$$\tilde{p} = \bar{p} + \bar{\rho} \tilde{T}. \quad (2.8)$$

The base states, as discussed in Lin *et al.* (2002), are given (in *dimensionless* form) as:

$$\bar{p} = \bar{\rho} = \bar{\rho}_o(y) \exp \left(-\frac{z^2}{2} \right), \quad (2.9)$$

$$\bar{\mathbf{v}} = \frac{3}{2} y \mathbf{x}, \quad (2.10)$$

where $\bar{\rho}_o(y)$ represents the radial variation of the base density, and \mathbf{x} is the unit vector in the x direction. The dimensionless base temperature, which is assumed to be constant, simply becomes $T_o = 1$. For the radiation time τ_{rad} , we currently assume the following dimensionless form,

$$\tau_{rad}(z) = \tau_o \exp(-z^2).$$

We set τ_o to be approximately 10^6 times that of the orbital period (denoted τ_{orb}). When such a value is assumed there is almost no radiative dissipation at the midplane, and the radiation time scale is comparable to the orbital period close to the upper and lower boundaries of the disk. The radiation scheme captures only the long term dissipative behavior of the disk, and has a negligible effect on dynamics that have time scales comparable with orbital periods.

Equations (2.5-2.8), together with appropriate boundary conditions, are the set of equations we solve numerically.

3. Numerical scheme

Before presenting in detail the numerical algorithm, it is appropriate to address a few of the special challenges involved in the system we are trying to solve. First, we have a base shear flow in a rotating frame as indicated by equation (2.10). For this kind of problem it is natural to think about a sliding-box formulation, as it has been implemented by Rogallo (1981) and Hawley *et al.* (1999). Two of the current authors (J.A.B. and P.S.M.) have also developed a similar algorithm to solve the system of equations (2.5–2.8) using the sliding-box methodology. In this sliding-box formulation, flow in the radial direction is artificially periodic after subtraction of the convection ensued from the base shear flow, and the vertical direction is represented in Chebyshev series to capture the non-periodic buoyancy (gravity) force. Nonetheless, because in the current code we aim to represent a non-periodic radial thermodynamic (potential-vorticity) background (see discussions in Lin *et al.* (2002)), we can no longer assume the artificial periodicity in y , and functions in this direction should be instead represented in Chebyshev series. This complication forces us to assume an artificial periodicity in the vertical direction under the current framework of a Fourier-Fourier-Chebyshev representation, and we shall have more discussions regarding this point later. Secondly, we account for density variation (albeit with a simplified form) *via* the anelastic continuity equation (2.6), and capture the stably-stratified physics through a vertically decaying density $\bar{\rho}$, a temperature (energy) evolution equation (2.7), and a buoyancy (gravity) force term in the momentum equation (2.5). Thirdly, because the base density has the fast-decaying form of equation (2.9) (*e.g.* at $z = \pm 3H_o$, the base density decays to only 1% of its value at the midplane), it should be carefully treated to avoid numerical instability. Finally, the coherent vortices we are trying to identify assumes full three-dimensional structures for reasons discussed in Barranco *et al.* (2000).

We solve equations (2.5–2.8) with a pseudo-spectral scheme. We represent functions in the x and z direction with Fourier series, and functions in the y direction by Chebyshev series. Because of the artificial periodicity in the z direction, we have to replace the variable z in the buoyancy force term $\tilde{\rho}z$ with a new periodic function z^* that equals z for most of the domain, but comes back to zero to enforce periodicity toward the upper and lower boundaries (see Figure 1). Because the base density $\bar{\rho}$ (and hence momentum, energy, *etc.*) becomes very small where z^* has the largest deviation from z , and because our vortices have a compact structure around $z = 0$, the influence of this replacement of z with z^* is assumed to be minimal.

For time integration we adopt a Leap-Frog scheme for calculation of the nonlinear terms. Our algorithm can be compactly written as

$$\hat{\mathbf{u}}^{M+1} = \mathbf{u}^{M-1} + 2\Delta t(\mathbf{n}^M - \tilde{\rho}^M z^* \mathbf{z}), \quad (3.1)$$

$$\nabla^2 \tilde{p}^M = \nabla \cdot \hat{\mathbf{u}}^{M+1}, \quad \left[\frac{\partial \tilde{p}^M}{\partial y} = \frac{1}{2\Delta t} \hat{u}_y^{M+1} \right]_{y=\pm 1}, \quad (3.2)$$

$$\mathbf{u}^{M+1} = \hat{\mathbf{u}}^{M+1} - 2\Delta t \nabla \tilde{p}^M, \quad (3.3)$$

$$T^{M+1} = (T^{M-1} + 2\Delta t n_T) e^{-2\Delta t/\tau_{rad}}, \quad (3.4)$$

where

$$\mathbf{u} \equiv \bar{\rho} \mathbf{v} \quad (3.5)$$

is momentum and our working variable, the superscript M denotes quantities at the M^{th} time step, \mathbf{n} is the sum of the nonlinear terms on the RHS of equation (2.5) excluding the

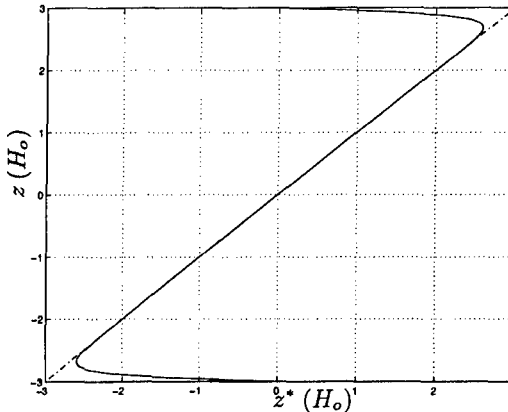


FIGURE 1. The artificially enforced periodic function z^* (solid), compared with the original linear function z (dash-dotted). In this plot the vertical domain extends from $-3H_o$ to $3H_o$; the value of the base density $\bar{\rho}$ at the upper and lower boundaries ($z \approx \pm 3H_o$) is about 1% of its value at the midplane ($z = 0$). Our vortex structure, as we shall present later, is compact in z and primarily assumes the domain from $-H_o$ to H_o .

buoyancy force, and n_T is the sum of the nonlinear terms on the RHS of equation (2.7) excluding the radiation term. The Helmholtz equation (3.2) is inverted to solve for pressure which consequently enforces the divergence free condition (2.6) at the $(M+1)^{th}$ step. In our code we have also implemented a τ -method that ensures equation (2.6) is satisfied for all Chebyshev modes. We found that the latter method improves numerical stability. For boundary conditions, we are currently implementing no-flow condition at $y = \pm 1$ (which is enforced by the pressure boundary condition when solving for \tilde{p}^M in (3.2)). The advantage of doing this is to contain our flow and enforce conservation laws within the computational domain. Finally we apply a 6th order hyperviscosity/hyperdiffusion on both the momentum and energy equations to ensure numerical stability.

Note that we have not adopted the more commonly practiced Adams-Bashforth (for nonlinear terms) and Crank-Nicolson (for pressure) time-integration scheme. This is because the current Leap-Frog scheme has better performance in terms of avoiding the instability caused by the large density variation of $\bar{\rho}$ in the vertical direction. Note also that when inverting the Helmholtz problem (3.2) for \tilde{p}^M , the \hat{u}^{M+1} term on the RHS contains a buoyancy term $\tilde{\rho}^M z^*$, in which the density $\tilde{\rho}^M$ is related to the pressure \tilde{p}^M via the equation of state (2.8). This coupling problem is resolved by an iterative method. We use $\tilde{\rho}^{M-1}$ as the initial value $\tilde{\rho}_0^M$ to enter the iteration on the RHS of equation (3.2). Once the pressure \tilde{p}_0^M is obtained by inverting the Helmholtz problem, it is used to obtain a new density function using

$$\tilde{\rho}_{i+1}^M = \tilde{\rho}_i^M - \bar{\rho} \tilde{T}^M, \quad (3.6)$$

which subsequently enters the Helmholtz solver as the new density. we found that ~ 5 times of this procedure give excellent convergence at an acceptable computational cost.

To improve the speed of the code we have also implemented a “faster” variation of our algorithm. This implementation is based on the following consideration. We can rewrite the momentum and energy equations as

$$\frac{\partial \mathbf{u}}{\partial t} = -\sigma y \frac{\partial \mathbf{u}}{\partial x} + \mathbf{n} - \nabla \tilde{p} - \tilde{\rho} z^* \mathbf{z}, \quad (3.7)$$

$$\frac{\partial T}{\partial t} = -\sigma y \frac{\partial T}{\partial x} + n_T - \frac{T}{\tau_{rad}}, \quad (3.8)$$

where $\sigma = \frac{3}{2}$ is the shear rate of the base flow, and \mathbf{n} and n_T are the same as previously defined. In this case, however, we further exclude the base-shear convection terms. The base shear flow poses a major constraint on the size of the time-step if calculated explicitly, whereas the flow structure we are interested in is only a small deviation from this base flow (Barranco *et al.* 2000). We therefore separate the base convective terms $-\sigma y \frac{\partial \mathbf{u}}{\partial x}$ and $-\sigma y \frac{\partial T}{\partial x}$ and treat them analytically. Our new algorithm, in which the base convection is represented in terms of waves, is written

$$\hat{\mathbf{u}}^{M+1} = e^{-2ic\Delta t} \mathbf{u}^{M-1} + e^{-ic\Delta t} 2\Delta t (\mathbf{n}^M - \nabla \tilde{p}^{M-1} - \tilde{\rho}^{M-1} z^* \mathbf{z}), \quad (3.9)$$

$$\mathbf{u}^{M+1} = \hat{\mathbf{u}}^{M+1} - 2\Delta t [\nabla(\tilde{p}^M - \tilde{p}^{M-1}) + (\tilde{\rho}^M - \tilde{\rho}^{M-1}) z^* \mathbf{z}], \quad (3.10)$$

$$T^{M+1} = (e^{-2ic\Delta t} T^{M-1} + e^{-ic\Delta t} 2\Delta t n_T^M) e^{-2\Delta t/\tau_{rad}}. \quad (3.11)$$

Here $c \equiv k_x \sigma y$, that is, these exponents are applied for each wave number k_x in the x direction and at each point y in the transverse domain. This formula assumes the form of a semi-implicit, predictor-corrector algorithm of second-order accuracy. Again a Helmholtz problem is solved to obtain pressure and enforce continuity equation, and an iterative method is used to simultaneous obtain \tilde{p}^M and $\tilde{\rho}^M$. In this new algorithm our effective flow number is calculated from

$$|\tilde{\mathbf{v}}| = |\mathbf{v} - \bar{\mathbf{v}}| \ll |\bar{\mathbf{v}}|.$$

Because the maximum value of $\tilde{\mathbf{v}}$ is typically only 1/5 that of $\bar{\mathbf{v}}$, we can use significantly larger time steps.

Our algorithms are implemented for parallel computation using MPI, with a communication algorithm for FFT provided by Dr. Alan Wray. We test and run our code on the *SGI Origin 2000* clusters at NASA Ames. We have performed diagnostics such as conservation of mass, momentum and energy. Aside from the results that we shall present below, we have also tested finer resolutions for convergence. We have followed the standard diagnostic procedures and the details shall not be presented here.

4. Results

We now present our computational results for three dimensional vortices. We shall be seeking the *existence* of three-dimensional, coherent vortices which can survive in an environment such as that of the protoplanetary disk. We will call these vortices henceforth “*equilibrium*” vortices.

Because we seek vortices that are in dynamic equilibrium with their environment, a natural approach would be to generalize the idea of the well-known Moore-Saffman vortices (see, *e.g.* Saffman (1992)) to three dimensions. In Lin *et al.* (2002) we have discussed columnar Moore-Saffman vortices, which are quasi-two-dimensional objects. In the following we present results for three-dimensional vortices, which resemble Moore-Saffman vortices in the horizontal planes, but have compact support in the vertical direction. Before we start it is useful to list the vorticity-aspect-ratio relation given by Moore-Saffman theory:

$$\frac{\tilde{\omega}_z}{\sigma} = \lambda \frac{\lambda + 1}{\lambda - 1}, \quad (4.1)$$

where $\tilde{\omega}_z$ is the strength of the constant vorticity patch superimposed on the shear, and $\lambda < 1$ is the ratio of the semi-axes of the elliptic patch.

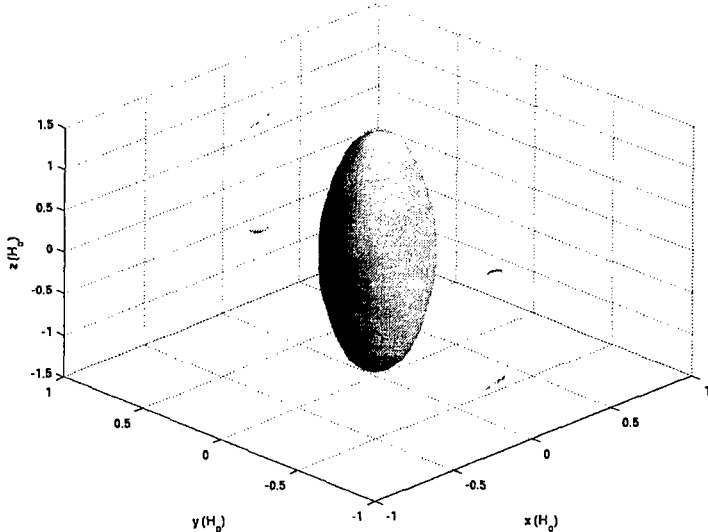


FIGURE 2. Three-dimensional vortex structure in the absence of shear. Here we show the iso-surface at the value $\tilde{\omega}_z = -1$, and at the time $t = 20 \tau_{\text{orb}}$. Our computational resolution is $128 \times 64 \times 96$ on a computational domain of $8 \times 2 \times 6$ (not entirely shown in this graph).

4.1. Vortices without shear

We first present a relatively simple case in which we set the shear to be zero, that is, $\sigma = 0$. This case will facilitate a comparison with our later results where we see the effects of a strong shear on the vortex. As the initial condition, we specify a vorticity function as

$$\tilde{\omega}_z = \begin{cases} \omega_o \exp\left(-\frac{z^2}{2}\right), & \sqrt{x^2 + y^2} \leq r_o \\ 0, & \sqrt{x^2 + y^2} > r_o \end{cases}, \quad (4.2)$$

where $\omega_o = -2.25$, $r_o = 0.25$ is the radius of the circular patches (note that from (4.1) $\lambda \rightarrow 1$ when $\sigma \rightarrow 0$), and the Gaussian distribution renders the vortex compact in z . We have set $\tilde{\rho}$ to give an initial hydrostatic balance in the vertical direction.

The vortex goes through a brief (on the scale of turn-around time) and slight adjustment and then evolves into an equilibrium shape that is coherent for many (we have tested up to 120) turn-around times. See Figure 2.

4.2. Vortices in a Keplerian shear

Similar to the case without shear, we start with an initial guess that is close enough to the equilibrium state. We specify our initial vorticity function as

$$\tilde{\omega}_z = \begin{cases} \omega_o \exp\left(-\frac{z^2}{2}\right), & x^2/a^2 + y^2/b^2 \leq 1 \\ 0, & \sqrt{x^2/a^2 + y^2/b^2} > 1 \end{cases}, \quad (4.3)$$

where $\omega_o = -0.625$, and the semi-axes are specified as $a = 0.25$ and $b = 1.0$. At the midplane $z = 0$, the elliptical vortex patch satisfied exactly the Moore-Saffman relation (4.1), and again the vorticity strength decreases with a Gaussian distribution away from the midplane. Similarly we have specified the initial $\tilde{\rho}$ such that the flow is in hydrostatic balance. Note that we have specified a lower value for ω_o . This is because J.A.B. and P.S.M. found that lower vorticity strength (albeit still of a moderate Rossby number)

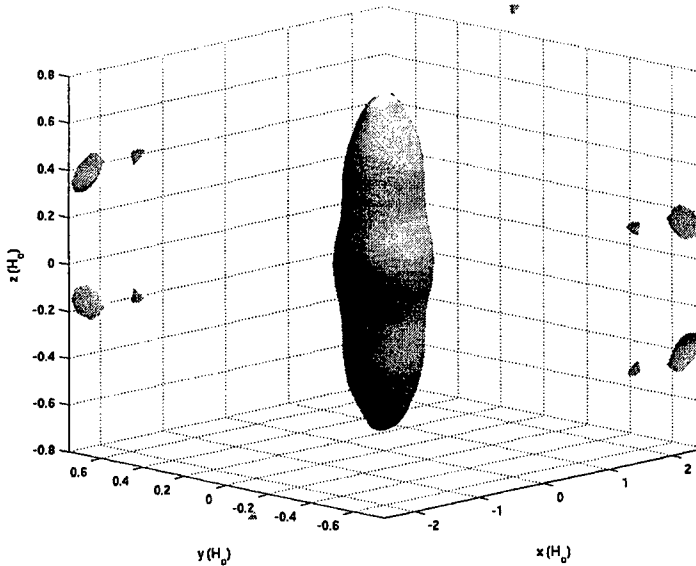


FIGURE 3. Elongated three-dimensional vortex structure in a Keplerian shear ($\sigma = 1.5$). Here we show the isosurface at the value of $\tilde{\omega}_z = -0.55$, and at the time $t = 20 \tau_{\text{orb}}$. Our computational resolution is $128 \times 64 \times 96$ on a computational domain of $8 \times 2 \times 6$ (not entirely shown in this graph).

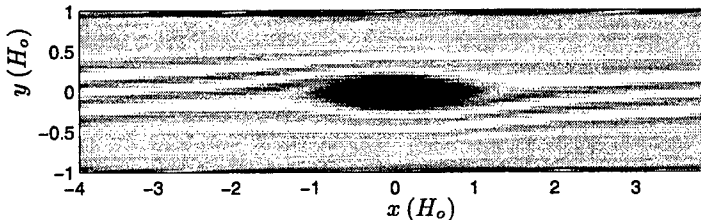


FIGURE 4. Contour plot of same vortex structure as shown in Figure 3 at the midplane $z = 0$. In this plot darker color designate the more negative values of $\tilde{\omega}_z$, and the black spot at the center is our equilibrium vortex patch. At the midplane the vortex is almost exactly Moore-Saffman.

induces fewer thermodynamic oscillations in the vertical direction and therefore aids coherence.

The resulting equilibrium vortex (after a few turn-around times from the initialization) is shown in both Figures 3 and 4. In Figure 3 we show an isosurface plot of the vertical vorticity $\tilde{\omega}_z$. When compared with Figure 2, the vortex is stretched by the shear and has a elongated shape in the horizontal directions (Figure 4).

Figure 5 illustrates the evolution of the vertical vorticity profile $\tilde{\omega}_z$ in time. The vorticity quickly adjusts, on turn-around-time scales, to an equilibrium distribution that is maintained for a much longer period. (We have tested up to 60 turn-around times in this case.) Note that, close to the midplane, the vorticity goes through small-amplitude oscillations. This is because at $z = 0$ there is no gravitation and the flow is at its least stably stratified.

Finally we compare our results (henceforth denoted as “current”) with those from a sliding-box implementation (denoted “sliding-box”) that has been developed by J.A.B.

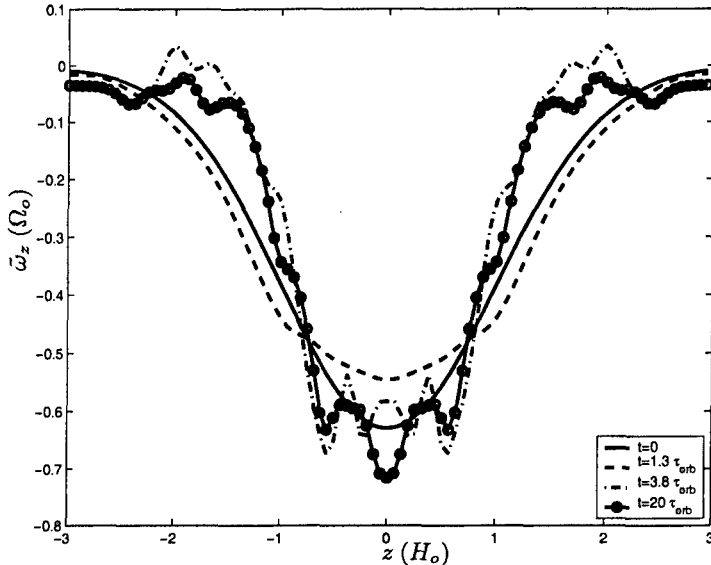


FIGURE 5. Time evolution of vertical vorticity profile $\tilde{\omega}_z(z)$ for vortices shown in Figure 3 and 4. The vorticity starts with a Gaussian distribution (solid), goes through quick adjustment (dash) and evolves into an equilibrium shape (dot-dash and line-circle).

and P.S.M. The most significant difference between these two codes lies in the boundary conditions. For the streamwise x direction, a natural periodicity is assumed for both methods. For the other two (transverse and vertical) directions, our current implementation has an artificial periodicity in z and enforces a no-flow condition in y , whereas the sliding box formulation assumes a shear-convected periodicity in y and a no-flow condition in z . The agreement between these two implementations is an important validation of the results from both.

In Figure 6 we show the comparison of the equilibrium vorticity $\tilde{\omega}_z$ along the three major axes. We initialize with the same vorticity distribution that is given by equation (4.3). The velocity, pressure and density functions are obtained satisfying both the hydrostatic balance and the boundary conditions in each of the implementations. The flows then evolve and we compare our results after 20 orbital periods. The results indicate excellent agreement between the methods.

The most significant difference lies in the vorticity distribution along the z axis. This difference can be better illustrated by a contour plot of $\tilde{\omega}_z$ along the $x = 0$ slice (Figure 7). The difference in $\tilde{\omega}_z(0, 0, z)$ is primarily manifested as a smaller vortex size in the current method. Nonetheless, the equilibrium shapes of these vortices agree well with each other, and, most strikingly, the black-and-white stripe patterns emanating away from the vortices are almost exactly reproduced in both of the methods, even though the boundary conditions are very different. These patterns are speculated to be gravity waves. Both the gravity waves and the difference in vortex size require more detailed study in the future.

5. Future Work

In the present paper we have shown the numerical implementation, as well as our results on three-dimensional, equilibrium vortices. We have compared and validated our

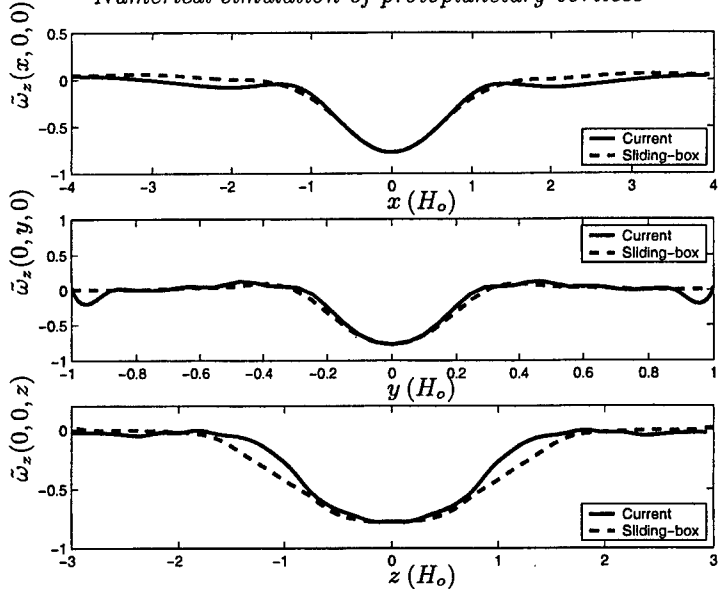


FIGURE 6. Comparison of equilibrium vorticity distribution against a sliding-box calculation along the three major axes of the vortex structure.

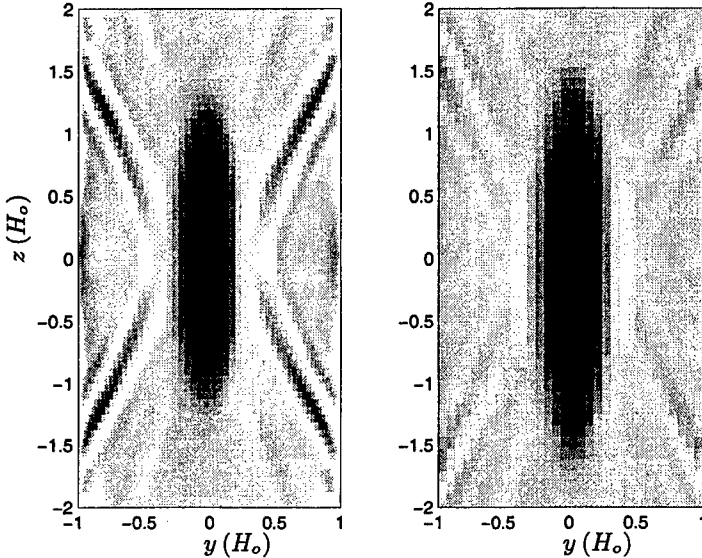


FIGURE 7. Comparison of equilibrium vorticity distribution against a sliding-box calculation. Here we plot the function $\tilde{\omega}_z(0, y, z)$, and the darker color correspond to the more negative values. The very black patches in the middle are our equilibrium vortex structures. Result from the current method is shown in the left graph, and that from the sliding-box method is shown to the right.

results with an alternative, sliding-box method. A few of the issues that we shall be immediately looking into next are as follows. First, even though we have identified a family of equilibrium vortices from one particular form of initialization, we should also seek other possible forms of equilibrium vortices. For example, we have tried the combi-

nation of different decaying exponents in (4.3) and different vorticity strength ω_o , and found equilibrium vortices under certain conditions. (This work is still in progress and is not presented here.) Second, we have preferred a no-flow condition in the y direction, primarily because of its advantage in diagnosing the conservation laws. This more rigid boundary condition should be relaxed or modified in the future to better reflect the physics of the disk. Finally, the purpose of the current numerical implementation has been to overcome the limitation of the sliding-box formulation, and eventually simulate a radial (y) thermodynamic (potential-vorticity) background. Our ultimate goal would be to generate coherent vortices from such a (baroclinic) background, as well as to study the dynamical migration and deformation of such vortices; with these achieved we will be ready to address their relevance to the greater problem of angular momentum and mass transport within protoplanetary disks.

Acknowledgments

H.L. thanks Dr. Karim Shariff and Dr. Alan Wray of NASA Ames for very constructive insights and discussions.

REFERENCES

- BARRANCO, J.A. & MARCUS, P.S. 2000 Vortices in protoplanetary disks and formation of planetesimals. In *Proceedings of the 2000 Summer Program*, 97-108. Center for Turbulence Research, Stanford University.
- BARRANCO, J.A., MARCUS, P.S. & UMURHAN, O.M. 2000 Scalings and asymptotics of coherent vortices in protoplanetary disks. In *Proceedings of the 2000 Summer Program*, 85-95. Center for Turbulence Research, Stanford University.
- HAWLEY, J.F., BALBUS, S.A. & WINTERS, W.F. 1999 Local hydrodynamic stability of accretion disks. *ApJ* **518**, 394-404.
- KLAHR, H.H. & BODENHEIMER, P. 2003 Turbulence in accretion disks: vorticity generation and angular momentum transport via the global baroclinic instability. *ApJ* **582**, 869-892.
- LIN, H., BARRANCO, J.A. & MARCUS, P.S. 2002 Vortex dynamics and angular momentum transport in accretion disks. In *Center for Turbulence Research Annual Research Briefs 2002*, 289-299. Stanford University.
- LOVELACE, R.V.E., LI, H., COLGATE, S.A. & NELSON, A.F. 1999 Rossby wave instability of Keplerian accretion disks. *ApJ* **513**, 805-810.
- ROGALLO, R.S. 1981 Numerical experiments in homogeneous turbulence. *NASA Tech. Mem.* **81315**, 1-91.
- SAFFMAN, P.G. 1992 *Vortex Dynamics*. Cambridge University Press.
- SHAKURA, N.I. & SUNYAEV R.A. 1973 Black holes in binary systems. Observational appearance. *Astron. Astrophys.* **24**, 337-355.
- STONE, J.M. & BALBUS, S.A. 1996 Angular momentum transport in accretion disks via convection. *ApJ* **464**, 264-372.